Bio-mimetic optical sensor for structural deflection measurement

Susan A. Frost*[a], Cameron H.G. Wright [b], Robert W. Streeter[b], Md. Arif Khan[b], Steven F. Barrett[b]
[a]NASA Ames Research Center, POB 1, M/S 269-3, Moffett Field, CA USA 94035;
[b]Dept. of Electrical and Computer Engineering, University of Wyoming, 1000 E. University Ave, Laramie, WY USA 82071

ABSTRACT

Reducing the environmental impact of aviation is a primary goal of NASA aeronautics research. One approach to achieve this goal is to build lighter weight aircraft, which presents complex challenges due to a corresponding increase in structural flexibility. Wing flexibility can adversely affect aircraft performance from the perspective of aerodynamic efficiency and safety. Knowledge of the wing position during flight can aid active control methods designed to mitigate problems due to increased wing flexibility. Current approaches to measuring wing deflection, including strain measurement devices, accelerometers, or GPS solutions, and new technologies such as fiber optic strain sensors, have limitations for their practical application to flexible aircraft control. Hence, it was proposed to use a bio-mimetic optical sensor based on the fly-eye to track wing deflection in real-time. The fly-eye sensor has several advantages over conventional sensors used for this application, including light weight, low power requirements, fast computation, and a small form factor. This paper reports on the fly-eye sensor development and its application to real-time wing deflection measurement.

Keywords: optical sensor, bio-mimetic, target tracking, fly-eye sensor, deflection measurement

1. INTRODUCTION

In an effort to reduce the environmental impact of aviation, lighter weight aircraft configurations are being considered [1]. One challenge of light weight aircraft wings is increased flexibility that can adversely affect handling qualities and safety. Approaches using active control to mitigate problems associated with flexible wings have been proposed [2]-[6]. Knowledge of aircraft wing position during flight can provide significant advantages to the effectiveness of these approaches. Current approaches to measuring wing deflection, including strain measurement devices, accelerometers, or GPS solutions, and new technologies such as fiber optic strain sensors, have limitations for their practical application to flexible aircraft control. Traditional machine vision systems using charge coupled device (CCD) or complementary metal oxide semiconductor (CMOS) arrays have several disadvantages for applications requiring high sensitivity to motion and high speed extraction of certain image features such as the object edges of a target, including the blurring of objects moving at high speed, and the high computation and data throughput requirements for edge detection [7]-[8]. A machine vision system that can perform high speed target tracking in near real-time with low power requirements is desirable for wing deflection tracking.

An optical sensor based on the physiological aspects of the eye (and vision-related neural layers) of the common housefly (*Musca domestica*) has been developed by researchers at the Wyoming Image and Signal Processing Research (WISPR) Laboratory at the University of Wyoming [9]-[16]. A bio-mimetic (also known as biologically inspired) engineering approach was used to extract salient features of the fly's visual system for use in the optical sensor. The intent of the research is not to completely reproduce the ability, appearance, or function of the fly's vision system. Rather, select features that are desirable in image processing are reproduced, including high functionality in low-light and low-contrast environments, sensitivity to motion, compact size, and low power and computation requirements.

*susan.frost@nasa.gov

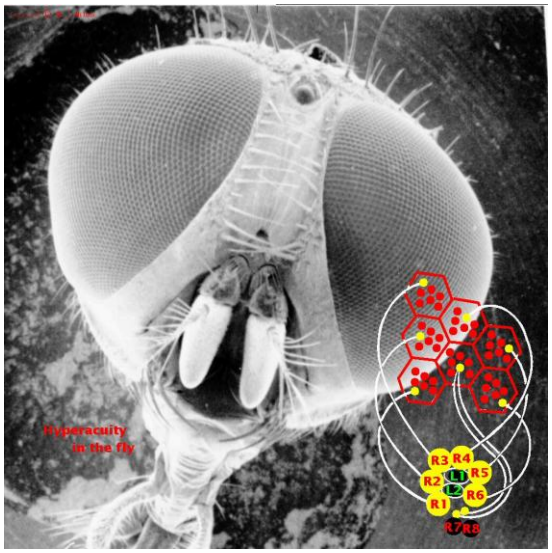

Fig. 1. Scanning electron microscope image of *Musca domestica*, with a depiction of the associated first layer neural "wiring" superimposed that shows neural superposition. *Image courtesy of M. Wilcox.*

There is a large body of research on the fly-eye visual system (see fig. 1) that was leveraged to develop the fly-eye sensor described here [16]-[20]. Laboratory tests were performed on flies at the University of Wyoming to characterize the arrangement and interaction of light sensitive cells (ommatidia) in the fly's compound eye [16]. The fly uses a combination of quasi-Gaussian overlapping photoreceptor responses and neural superposition to achieve what has been described in the literature as "hyperacuity," or the ability to detect image features, such as object motion, to a much higher degree than just the photoreceptor density would imply. See fig. 2 for an image depicting the overlapping Gaussian visual field of three photoreceptors. The overlapping and quasi-Gaussian response fields-of-view (FoVs) allow for very precise and very fine measurements of position, direction, and speed.

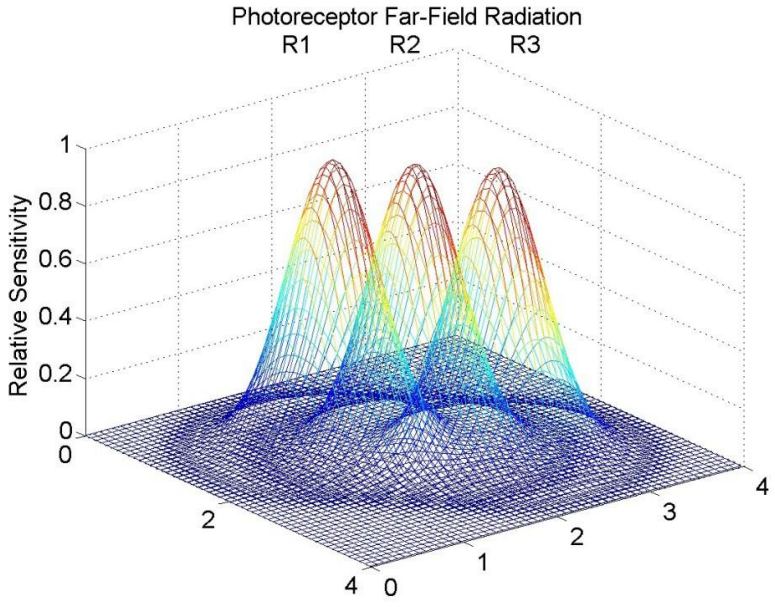

Fig. 2. Depiction of overlapping Gaussian response similar to that exhibited by the compound eye of common house fly.

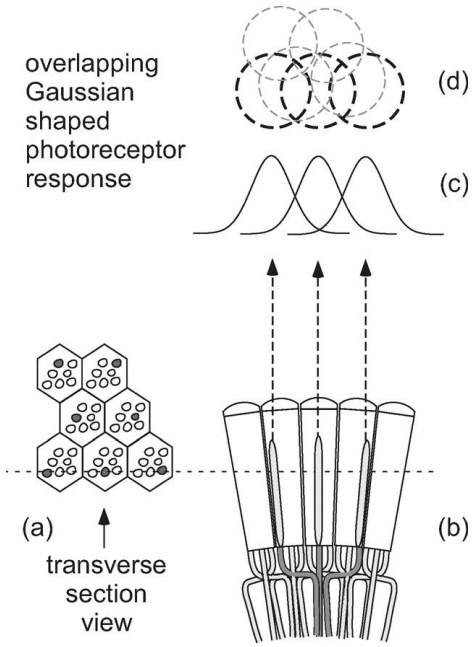

Fig. 3. Simplified diagram showing Gaussian overlapping photoreceptor response and neural superposition of fly-eye visual system; each hexagonal shape in (a) delineates the cross section of a structure called an ommatidium.

Figure 3 shows a simplified diagram to illustrate the quasi-Gaussian (henceforth called simply "Gaussian") overlapping photoreceptor response and neural superposition that both contribute to such desirable sensor capabilities. In this figure, the seven shaded photoreceptors from seven physically distributed ommatidia (the structural elements that make up an insect's compound eye) shown in (a) all view the same point at infinity. The overlapping visual field of the three receptors depicted in (b) is shown as (c). All seven visual fields (as half power radii) are shown perpendicular to the optical axis in (d). Signals from the physically distributed but optically coaligned photoreceptors combine in the neural layer and together are called a "cartridge." While the fly has eight photoreceptors in each ommatidium, (fig. 1), receptors R7 and R8 are "stacked" and share a single optical axis. Note that the Gaussian overlap for an artificial sensor comes from the front-end optical design, whereas the neural superposition is accomplished by how the signals are subsequently combined.

Since the sensor excels in detection of even minute motion, a feasibility study using the sensor for detailed target tracking was proposed. The purpose is to track a known target pattern at relatively short range, and resolve the position and velocity of the pattern relative to a neutral position. One application is the precise measurement of wing deflection in a fixed wing aircraft. This optical approach allows for a faster, more efficient approach than alternative methods (such as accelerometers or strain gages within the target object). This method does have drawbacks however, such as its reliance on a clean line-of-sight to the target.

2. SENSOR DESIGN & CONSTRUCTION

2.1 Sensor Subsystems

This section describes the function and composition of each subsystem within the fly-eye sensor as designed by Dean [12], which includes lessons learned from several years of development by other researchers [9]-[16]. See fig. 4 for a block diagram of the functionality of one fiber optic channel of the sensor from input to output. The version of the sensor described here uses seven fiber-optically fed IFD91 photodarlington detectors [21]. These semiconductive devices output a current proportional to the number of photons impinging on the element (i.e. the quantity of light in front of the element). This current is small (on the order of 0.1 μA to 10 mA) and thus requires both conversion to a voltage as well as amplification. Following the photodarlingtons, a logarithmic compression amplifier circuit is used to achieve current-to-voltage conversion and to enable increased dynamic range of the output values. Use of the sensor in a wide variety of ambient lighting conditions, such as from dim light to extremely bright conditions, requires such increased dynamic range to ensure adequate image contrast for detection purposes.

Fig. 4. Block diagram of sensor functionality through a single channel, where *i* represents current and *v* represents voltage.

A set of active filters are used to remove noise present in the signal. These filters include a 4th-order Butterworth low-pass filter with a 50 Hz cutoff frequency and a notch filter centered at 60 Hz. These filters specifically target noise sources that manifest themselves as flicker in interior lighting, which is well within the detection range of the sensor. This is an inexpensive, efficient filtering approach that requires only a small number of components and very little space on the PCB. Since the signal of interest is in the near-DC range, a low-pass filter is used.

Light adaptation makes use of the average value of the ambient lighting. The signal average is computed using a single-stage averaging amplifier arrangement. This circuit is a variation on a noninverting summing amplifier circuit, in which the gain for the signals coming from all 7 optical axes is set to approximately 1/7. The computed average is then filtered to near DC using a single stage active filter. This filter reduces oscillations caused by detected motion in the computation of the average, and thus mitigates the carry-over of those oscillations into the sensor output signals. The filter is only applied to the computed average value, and is not present in all 7 signal channels. The average is designed to accommodate all seven channel voltages. If a particular application requires fewer sensor channels (such as mono-axial tracking), and the sensor needs to be manufactured as inexpensively as possible, this circuit can be redesigned.

Following computation of the average value, an instrumentation amplifier is used to subtract the average from each of the 7 signals independently. This operation achieves what is referred to as "light-adaptation" through mean removal, a process by which the sensor can adapt to different levels of ambient lighting [12]. A low-power instrumentation amplifier is used to perform this subtraction. The outputs from this stage are considered the final sensor output signals, which can then be sampled by a computer.

Used by itself, the light adaptation circuit reacts almost instantaneously, which is detrimental to the sensor performance. Light adaptation is meant to adjust for relatively slow changes in ambient lighting to allow a wider dynamic range of operation than would otherwise be possible. It was found, not unexpectedly, that if the light adaptation is allowed to be too fast, it will "adapt" to light changes due to objects of interest instead of to ambient lighting, and make objects of interest harder to detect. The solution is to add a time delay to the light adaptation subsystem. All biological creatures incorporate such a time delay into their light adaptation physiology.

Traditional electronic time delay methods, such as memory/shift registers, are not feasible due to the need to preserve the analog nature of the signal. A method employing analog-to-digital conversion followed by a delay followed by digital-to-analog conversion would be too expensive in terms of computation power and time and it could introduce too much quantization error. Older analog methods such as resistive-capacitive (RC) or resistive-inductive (RL) delay lines suffer from poor stability and unrealistic component values for the delay needed, which was determined to be approximately one second. The resulting solution includes a sample and hold circuit with a timer that samples the analog signal, but does not quantize or digitally encode the signal. Thus delay was achieved without compromising the analog nature of the sensor signal [12].

2.2 Sensor Platform

A block diagram incorporating all of the above mentioned subsystems is provided in Fig. 4 and represents the sensor platform. A photodarlington pair produces a current (denoted by *i*) that is fed into a logarithmic compression amplifier. The output from that stage is a voltage (denoted by *v*), which is filtered, and the mean is removed as a form of light-adaptation. Figure 4 represents a single channel of a seven-channel system, and this process occurs in parallel for each channel. A printed circuit board (PCB) layout of the sensor circuits and components described above was designed and the board was built using industry standard reflow techniques [17].

Fig. 5. Front view of sensor head with U.S. dime for comparison.

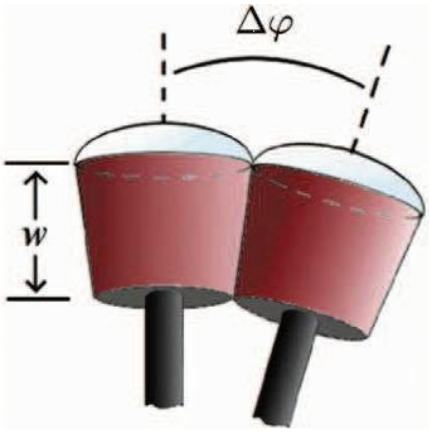

Fig. 6. Detail of two photo receptors in sensor head, where w represents the distance between the lens and the image plane and Δ φ represents the angle between two lenses.

The housing for the sensor head is the result of several iterations of development [9]-[16]. The version of the sensor being described here has an optically optimized dime-sized sensor head, see fig. 5. The sensor head housing was optimized with respect to response, motion acuity, and scalability for commercial production of the sensor, and it was designed to incorporate the multi-aperture nature of the *Musca domestica* eye. Results of the optimization suggested an ideal distance between the lens and the image plane of about w = 2.4 mm for pre-blurring, and an inter-lens angle of $\mathbf{\Delta\,\varphi}$ = 7.5 deg for 50% overlap, shown in fig. 6. The sensor head is a circular housing that is reasonably simple to manufacture and facilitates the tessellation of the sensors on a spherical surface. The circular housing holds seven lenses and seven optical fibers. The head is machine milled aluminum, with 1 mm, multi-modal, single-fiber optical light guides connecting it to the circuit board. The 3 mm lenses focus the incoming light onto the terminating ends of the light guides. To ensure the guides are the correct distance from the lenses, a specially designed tool is inserted into the housing and provides a temporary solid plane the guide can rest against until it can be secured in place. When all seven light guides and lenses are secured to the sensor head housing, and the guides are properly connected to the PCB, the sensor is considered fully assembled.

Once the sensor is physically assembled, it must be properly calibrated within the desired test environment. The sensor is calibrated by directing all facets toward an evenly lit, single-color, specular reflection free background and then adjusting the 50 kΩ potentiometers so that all outputs (one from each of the seven channels) are as near to the same value as possible. In an ideal lab setup, a curved Lambertian surface would be used to ensure that each of the seven channels is receiving stimulus that is not dependent on the viewing angle. This arrangement cannot be achieved with the

facilities available, so an alternative approach is used. The maximum output voltage difference measured after calibration in the lab is approximately 0.682 volts (about 5.4% of full-scale). An automatic calibration technique using digital potentiometers can also be used [12].

A hyperacuity to motion is a compelling attribute of this sensor package, and is one of the main reasons for this research. As a target moves within the FOV of the sensor, the response is nearly immediate. The photodarlingtons measure the quantity of light within their range. For example, a target that is darker than the background causes a decrease in the output of a photodarlington sensing the target. Tracking multiple outputs at once allows for the determination of the direction and speed of such a target.

Table 1. Characterization parameters for sensor measured over numerous trails.

Parameter	Min	Typical	Max
Output [V]	~0.0	0.49	0.72
Mean Voltage [V]	1.15	4.92	7.7
Operating Range [cm]		25.4	~130-150
Sensor, PCB, and Cables Weight [g]		135	
Input Illuminance [lx]	1	520	36,000
Power Consumption [W]		3.3	

Characterization tests have indicated a number of operating parameters for the system, see Table 1. These describe general operating conditions for the sensor package. Extreme conditions may result in different behavior. Note that, for all the methods and results discussed later, these parameters are taken into careful consideration. The logarithmic compression system is designed to operate up to 72,000 luminance (or lux) [12] , which, as Table 1 indicates, is far above the highest generated in the lab setting. The lux is measured using a Lutron LX-102 light meter. Current and voltage parameters are simultaneously measured using two Mastech MS8050 Digital Multimeters. While the operating range between the sensor and the target indicated in Table 1 is sufficient for the demands of this project, augmented range may be realized by using additional optics in front of the sensor head. The need for such optics is application specific.

3. TEST SETUP

A light box was constructed to enable controlled lighting for testing. The light box features a 48.5 in wide by 33 in tall by 56 in deep region for testing. In order to allow ambient room light to enter the box and to allow researchers to manipulate equipment within the environment, the top of the box is intentionally left uncovered. All interior surfaces are covered in a matte white felt that provides a uniformly, approximately Lambertian surface as a background. The sensor is mounted at one end of the box, and the target is placed within the box. All measurement, power supply, and analysis hardware is located immediately next to the box. Precision controlled light panels are used to control the light environment. These devices are constructed in-house to provide even “pure-white” light from Super Flux White Light-emitting Diode (LED) Lamps to illuminate the test environment. For the majority of the tests discussed here, ambient room light was sufficient and the panels were not needed.

Having a static target is desirable for fundamental device characterization tests; however, for target tracking, the presence of a dynamic target was necessary. A Houston Instrument plotter has been used for years at the University of Wyoming to facilitate dynamic tests [10]-[15]. The same device is used here to allow vertical oscillation of the target. The plotter is controlled using a Wavetek function generator. The function generator produces a triangular wave with an approximately known frequency and the plotter moves accordingly.

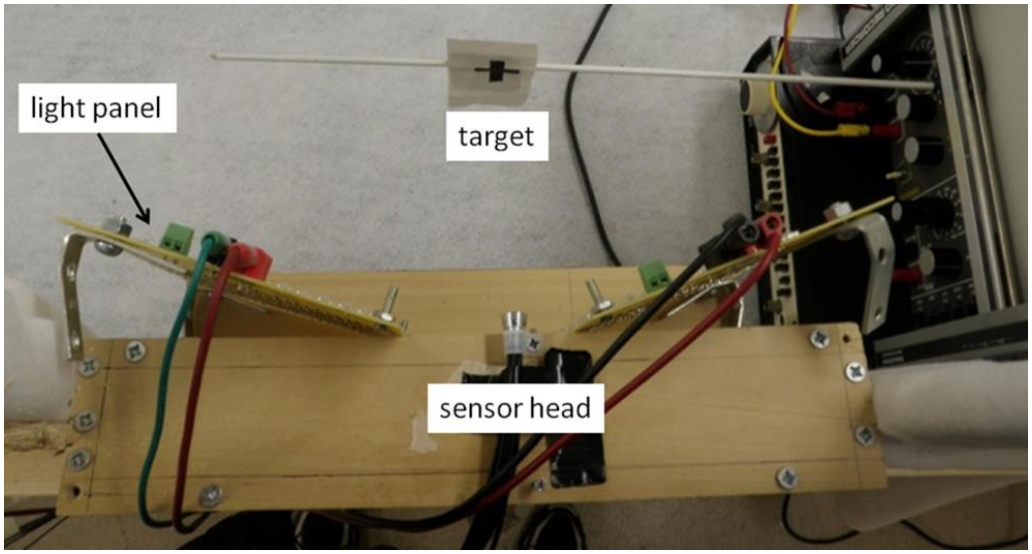

Fig. 7. Sensor head mounted in test box with target and light panel.

The sensor mount holds the sensor head stationary while tests are being conducted, but also allows for repositioning of the sensor between tests if the need arises, see fig. 7. A portion of the light-box wall is removed to provide the sensor mount a slot to reside within. This ensures the fiber-optic lines leaving the sensor head can smoothly connect to the PCB, and that the sensor and test hardware can be carefully manipulated by researchers. Figure 7 shows the sensor head on the mounting platform. The light panels appear on the left and right sides of the sensor head, the plotter appears on the right side of the figure, and the target itself (a "+" sign measuring 3 cm tall and 3 cm across) is just visible in front of the sensor head. See fig. 8 for an image of the target.

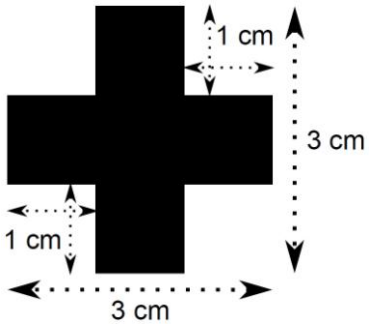

Fig. 8. Image of target used for testing.

The entire system (including the sensor itself) is powered by Mastech power supplies. Each light panel has its own supply, enabling adjustment of each panel separately. The sensor has a dedicated Mastech HY3005D-3 DC Power Supply that provides the necessary 15 VDC. Data is acquired through a DATAQ USB data acquisition unit (DAQ). This plug-and-play device utilizes the WinDAQ software package to simultaneously sample all seven DC voltages from the sensor. The program produces comma delimited .csv files. In all cases considered, the data is sampled at 30 Hz on each channel, which is close to the sampling limit of the DAQ.

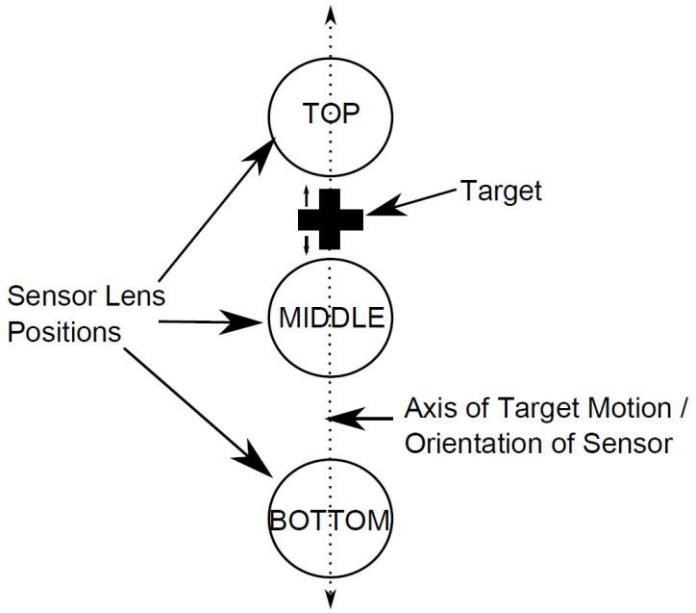

Fig. 9. Alignment of the sensor's primary axis and the motion axis of the target. Note that the target is not to scale.

Tests were performed using the setup described above. The motion of the target was strictly in the vertical direction, and along the central axis of the sensor. The alignment of the target and the sensor is illustrated in fig. 9. The "TOP," "MIDDLE," and "BOTTOM" labels refer to the positions of the lens relative to the rest of the test environment. In future discussions of the target tracking algorithm, these labels will be used to denote signals measured from the corresponding photodarlington.

The variable being altered from one test instance to the next is the oscillation frequency of the target. Numerous tests were performed, but the hardware used to create motion (the plotter) is limited to frequencies under approximately 0.8 Hertz. As a measure of the position truth, the waveform generated to drive the plotter is captured alongside the sensor data. This voltage acts as the reference to which reconstruction attempts are compared.

4. SOFTWARE TRACKING ALGORITHMS

A primary goal when designing software to accompany the fly-eye sensor is to use as simple an algorithm as possible for target position reconstruction. This ensures the algorithm has limited assumptions and maintains a minimal computational overhead cost. Initial attempts at position reconstruction presented here are offline techniques instead of a real-time algorithm that is ultimately desired. Offline approaches have the distinct disadvantage of having to post-process data from the sensor after the test is complete. It is expected that the offline approach will lead to a real-time implementation in the future.

The first step in the post-processing is to scale the data sets. Scaling is done by subtracting the difference between each individual channel mean and the minimum channel mean from each signal. Only three channels are used for this application, those associated with the three photodarlingtons along the sensor's primary axis. Thus, the TOP, MIDDLE, and BOTTOM measurements are moved into approximately the same range without corrupting any of the data. The position truth measure is also scaled into a similar range for display purposes.

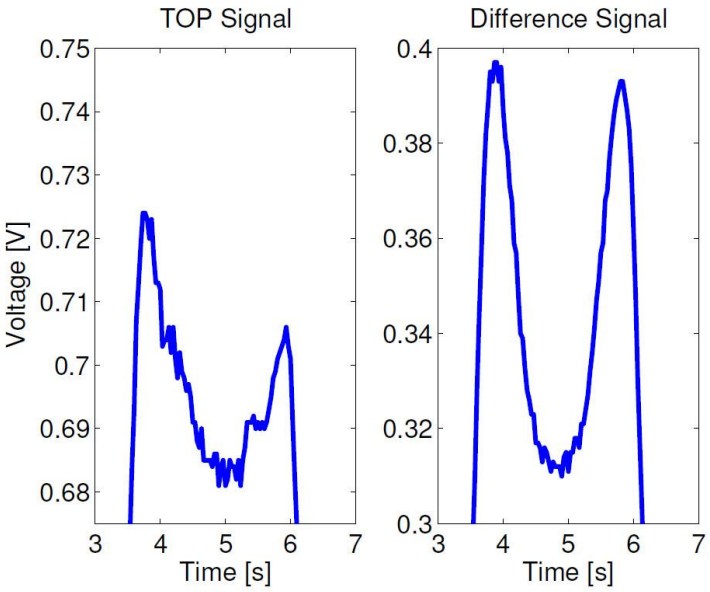

Fig. 10. Quantitative noise comparison of the scaled TOP signal and the difference signal.

Following the scaling procedure, the difference between the BOTTOM and TOP signals is computed. This value is the basis for the analysis and reconstruction. Using a difference signal provides the distinct benefit of common-mode noise removal. This reduction of noise can be qualitatively seen in fig. 10, which shows a zoomed view of the peaks in the raw TOP signal data and the TOP minus BOTTOM difference signal.

The eventual goal of this project is the creation of a frequency-independent, low-cost, low-power use, low-computational overhead tracking algorithm to use with the current generation of fly-eye sensor. The following algorithm, while still operating offline, simulates the behavior that could be achieved with a real-time algorithm. As with many real-time processing tasks, there is a transient start-up time during which the algorithm might not give proper reconstruction. The extent of this transient is not necessarily evident in this simulation, but the final tracking results are congruent with those that could be expected while operating fully in real-time.

The algorithm reported here uses the difference between the TOP and BOTTOM signals as a data source. The data is read into MATLAB™ from a .csv file, and then scaled for display purposes (this scaling is done to both the position data and the raw signal data). Next, the difference between the TOP and BOTTOM signals is computed. This is a process that can easily be done in hardware by using an instrumentation amplifier (such as an AD620). This difference is then smoothed using a 5-point moving average filter, as given by eq. (1)

$$y(i) = \frac{1}{5} \sum_{k=i-2}^{i+2} x(k) \tag{1}$$

where x is the original, unsmoothed data and y is the smoothed data. While the discrete nature of a 5-point moving average filter inherently demands digitization of the signal, a similar smoothing can be achieved using an analog low-pass filter. Since the algorithm's output very closely resembles the motion of the target itself, if the maximum oscillation frequency of the target is known, then the cutoff frequency of the filter can be set. An initial value could be 8-10 times the maximum target movement frequency. However, it is entirely possible to disregard this filtering if the high-frequency noise is low enough. The result of smoothed and unsmoothed approaches is given in the next section.

5. RESULTS

The results of the tracking algorithms previously discussed are provided and analyzed here. The eventual goal of the project is the development and deployment of an embedded system for the inexpensive, efficient, real-time measurement of wing deflection. These results are evaluated based on that goal. While the final results are given in units of voltage,

they can easily be mapped into different units (such as displacement distance), depending on the downstream requirements.

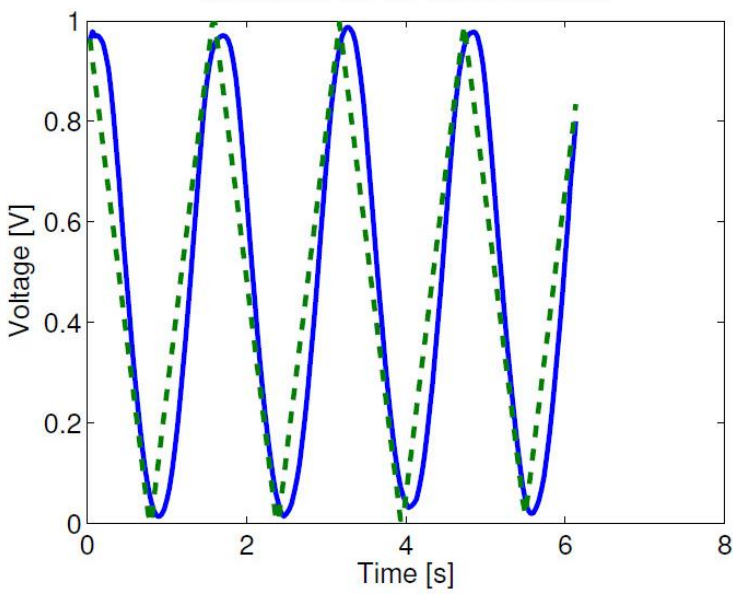

Fig. 11. Position reconstruction with smoothing for target oscillating at 0.2 Hz (solid line) and position truth (dashed line).

The resulting reconstruction of a target moving at 0.2 Hz is shown in fig. 11. As mentioned earlier, a delay is built into the sensor response to avoid artifacts in the signal. Additionally, since the X-Y plotter used to move the target is a mechanical system, there is some inherent delay within the device. Combined, these delays are evident in the figures illustrating the reconstructed position and the position truth. While compensation for this approximately 133 ms delay could be done, it would require additional computational overhead, and would likely be a frequency dependent process, something this algorithm strives to avoid. When conducting an error analysis of the reconstruction, specifically a mean squared error (MSE) based analysis, it is beneficial to remove this time delay by shifting the data into sync with the position truth. This avoids corrupting MSE-based error results.

Table 2. Fundamental error analysis of the reconstruction of 2.0 Hz target motion.

Parameter	**Value**
Mean squared error	0.0049
Root mean squared error	0.0697
Maximum error	0.1161
Average error	0.0624

Table 2 provides fundamental error statistics concerning the shifted reconstruction using the offline approach for the 0.2 Hertz data. Tests using a target moving at 0.8 Hz demonstrated similar error statistics. Since the values are scaled into the zero-to-one (0-1) range, an error of 1 would indicate the worst possible reconstruction value.

The optimal range for the target motion refers to the area in the sensor's FOV in which the overlapping nature of adjacent photodarlington responses is utilized. While motion primarily in a single channel's FOV does register a response from the sensor, hyperacuity depends upon multiple channels observing the motion. In addition, if the target moves beyond the center of the TOP or BOTTOM FOV, then the target position cannot be easily resolved with this technique due to the lack of an overlapping FOV in this area.

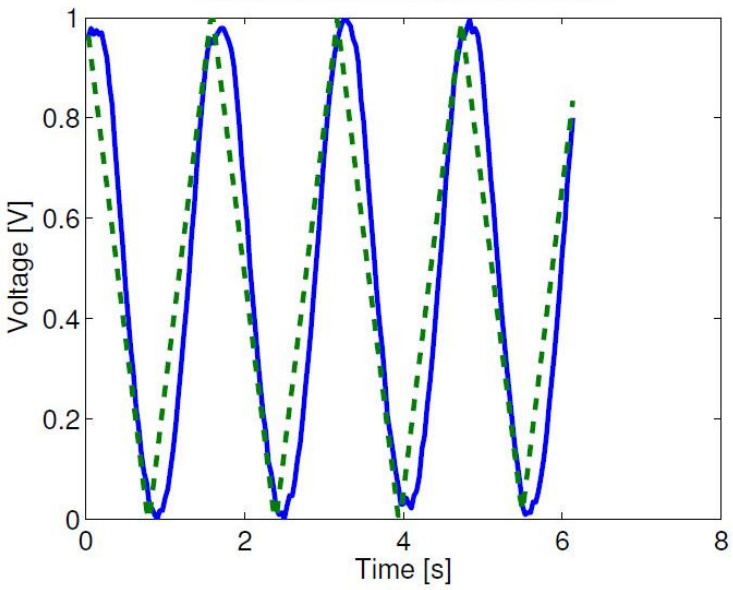

Fig. 12. Position reconstruction with no smoothing for target oscillating at 0.2 Hz (solid line) and position truth (dashed line).

While fig. 11 shows results using the algorithm that includes smoothing in the result, that step is not entirely necessary. Figure 12 shows results from the same 0.2 Hz test with the same algorithm except for the omission of the 5-point moving average filtering.

6. CONCLUSIONS

This paper reports on efforts to develop a bio-mimetic fly-eye sensor to track a target for real-time measurement of wing deflection. The fly-eye sensor has several advantages over conventional sensors used for this application, including light weight, low power requirements, fast computation, and a small form factor. A PCB was built for the sensor package as part of this research. Tests were run in which data was obtained from the sensor when a target moved in a vertical direction in front of the sensor. Algorithms that worked on the data after it was post-processed showed good target tracking results. Suggestions were made as to how these algorithms could be implemented in hardware to provide a real-time solution to target tracking the deflection of an aircraft wing.

ACKNOWLEDGEMENTS

This work was supported in part by the NASA Aeronautics Research Institute (NARI) and by grant number NNX12AP80A from NASA Ames Research Center.

REFERENCES

[1] NASA Aeronautics Research Mission Directorate, [Online]. Available: http://www.aeronautics.nasa.gov/, Jan. 27, 2014.

[2] L. Librescu, and P. Marzocca, "Advances in the linear/nonlinear control of aeroelastic structural systems," *Acta Mechanica* 178.3-4 (2005): 147-186.

[3] M.J. Brenner, R.C. Lind, and D.F. Voracek. *Overview of recent flight flutter testing research at NASA Dryden*. Vol. 4792. National Aeronautics and Space Administration, Office of Management, Scientific and Technical Information Program, 1997.

[4] A. Derkevorkian, S. F. Masri, J. Alvarenga, H. Boussalis, J. Bakalyar, and W. L. Richards, "Strain-Based Deformation Shape-Estimation Algorithm for Control and Monitoring Applications", *AIAA Journal*, Vol. 51, No. 9 (2013), pp. 2231-2240, doi: 10.2514/1.J052215.
[5] P.M. Suh and D.N. Mavris, "Modal filtering for control of flexible aircraft", *Proceedings 54th AIAA/ASME Structures, Structural Dynamics, and Materials Conference*, Boston, MA, April 2013.
[6] P.M. Suh, A.W. Chin, and D.N. Mavris, "Virtual Deformation Control of the X-56A Model with Simulated Fiber Optic Sensors," *Proceedings AIAA Atmospheric, Flight Mechanics Conference*, Boston, MA, Aug. 2013.
[7] G. C. Holst, *Electro-Optical Imaging System Performance*, 3rd ed. SPIE Press, 2003.
[8] R. H. Vollmerhausen, D. A. Reago, Jr., and R. G. Driggers, *Analysis and Evaluation of Sampled Imaging Systems*, SPIE Press, 2010.
[9] J. D. Davis, S. F. Barrett, and C. H. Wright, "Bio-inspired minimal machine multi-aperture apposition vision system," *ISA Biomedical Sciences Instrumentation*, vol. 44, 2008, pp. 373–379.
[10] D. T. Riley, W. Harman, S. F. Barrett, and C. H. G. Wright, "*Musca domestica* inspired machine vision sensor with hyperacuity," *IOP Journal of Bioinspiration & Biomimetics*, vol. 3, no. 2, Jun. 2008.
[11] J. B. Benson, C. H. G. Wright, and S. F. Barrett, "Redesign and Construction of an Artificial Compound Eye Visual Sensor," *ISA Biomedical Sciences Instrumentation*, vol. 44, pp. 367–372, Apr. 2008.
[12] B. Dean, "Light adaptation and applications for a fly eye vision sensor," Ph.D. dissertation, University of Wyoming, 2012.
[13] G. P. Luke, C. H. G. Wright, and S. F. Barrett, "A multiaperture bioinspired sensor with hyperacuity," *IEEE Sensors Journal*, vol. 12, no. 2, pp. 308–314, February 2012.
[14] R.W. Streeter, "Target tracking with a *Musca domestica* based sensor platform," M.S. thesis, University of Wyoming, 2013.
[15] R. S. Prabhakara, C. H. G. Wright, and S. F. Barrett, "Motion detection: A biomimetic vision sensor versus a ccd camera sensor," *IEEE Sensors Journal*, vol. 12, no. 2, pp. 298–307, February 2012.
[16] E. Tomberlin, "Musca Domestica's large monopolar cell responses to visual stimuli," Master's thesis, University of Wyoming, June 2004.
[17] K. Nakayama, "Biological image motion processing: A review," *Vision Res.*, vol. 25, pp. 625–660, 1985.
[18] J. S. Sanders and C. E. Halford, "Design and analysis of apposition compound eye optical sensors," *SPIE Optical Engineering*, vol. 34, no. 1, pp. 222–235, Jan. 1995.
[19] M. F. Land and D. Nilsson, Animal Eyes. Oxford, U.K.: Oxford Univ. Press, 2002.
[20] B. G. Burton and S. B. Laughlin, "Neural images of pursuit targets in the photoreceptor arrays of male and female houseflies Musca domestica," *J. Exp. Bio.*, vol. 206, pp. 3963–3977, 2003.
[21] Plastic Fiber Optic Photodarlington, Industrial Fiber Optics, Inc., 2006. [Online]. Available:http://www.fiberoptics.com/